In-situ Measurements of Temperature Distributions in a Microwave-Heated Cavity

Timothy Finegan, Paul E. Laibinis, and T. Alan Hatton
Dept. of Chemical Engineering, Massachusetts Institute of Technology, Cambridge, MA 02139

DOI 10.1002/aic.10897
Published online June 27, 2006 in Wiley InterScience (www.interscience.wiley.com).

The application of microwave heating technology to chemical processes outside of the food industries has been limited by an incomplete understanding of the temperature distributions formed within a microwave-heated cavity. A fluorescence-based optical method of thermometry is described for the in situ measurement of temperature distributions during microwave heating processes. Highly nonuniform, two-dimensional (2-D) temperature-distribution profiles were measured by resolving spatial variations in the fluorescence response of a temperature sensitive dye, Rhodamine B. The dye was excited by illuminating a slice within the sample cell using a planar expanded laser beam. Significant variations in the heating profiles of water and of salt (NaCl) solutions of different concentrations were observed, consistent with the influence of salt concentration on the dielectric properties of the solutions. The experimentally observed spatial variations in temperature before the onset of convection were in good agreement with predictions using a simple model to describe the electric field distributions in the microwave cavity. © 2006 American Institute of Chemical Engineers *AIChE J,* 52: 2727–2735, 2006
Keywords: microwave heating, temperature distribution, planar laser induced fluorescence

Introduction

Microwave heating technology has been an important development for the consumer sector, where microwave ovens can be found in the kitchen of nearly every home. The industrial success in applying microwave heating technologies has been far more limited, however, with the majority of industrial microwave heating installations being employed in food processing.[1] This limited deployment of microwave heating into the broader chemical industries is at odds with the commercial success of the household microwave oven, where it seems to offer the advantages of an ideal heat source, in its ability to dispense volumetric heating rapidly and with an instant control over the power it delivers to a system.[2] The use of microwave heating in industrial applications outside of the food industry has been limited in part to the lack of proven models of microwave heating that can be applied to industrial processes in the chemical industry. A goal of our work was to provide the first *in-situ* real-time experimental measurements of temperature distributions within a microwave-heated solution, and to validate experimentally the effects of solution properties on the predicted temperature distributions in these solutions. We used salt solutions of differing concentrations as a simple way to manipulate the dielectric properties of the solutions in our experiments, and observed spatial and temporal variations in temperatures upon their irradiation with microwaves—including the presence of definable nodes—that agreed well in position and in relative intensity with predictions based on equations of microwave absorption and heat transfer.

The heating of a material by microwave radiation occurs through dielectric polarization and relaxation processes. A polar molecule will align with its dipole along the direction of an applied electric field, and, if the field is oscillating, the molecule must rotate continually to maintain its alignment with the reversing direction of the field lines. For slow oscillations, the dipole is able to follow the changes in the field faithfully, but

Correspondence concerning this article should be addressed to T. A. Hatton at tahatton@mit.edu.
Current Address of T. Finegan: U.S. Air Force Research Laboratory Electro Optic Sensors, AFRL/SNJM Bldg. 622, 3109 Hobson Way St., WPAFB, OH 45433-7700
Current Address of P. E. Laibinis: Dept. of Chemical Engineering, Vanderbilt University, Nashville, TN 37235

if the oscillation is extremely fast, the molecule lacks sufficient time to respond to changes in the field and will in effect remain stationary. When the oscillation frequency is in the range of the dipolar response time, the molecule will respond to follow the field, but its alignment will lag behind the field direction. Since the molecule cannot dissipate the energy from the alignment forces, it must absorb the energy and consequently heat up.[3,4] The susceptibility of a material to dielectric polarization, and hence its propensity to absorb microwave radiation, is dependent on its dielectric properties as given by the complex dielectric constant

$$\varepsilon^* = \varepsilon' + i\varepsilon'' \tag{1}$$

The real part of this equation ε', is often tabulated as the (static) dielectric constant of a material and reflects the polarity of the molecule. The imaginary term ε'', is referred to as the dielectric loss, as it determines the extent of energy loss in an irradiated system through dipolar relaxation, and, hence, the overall heating rates in the system.[5] Both components of the dielectric constant are frequency and temperature dependent, and have been studied extensively for salt-water solutions[6–11] and mixtures of polar organic solvents.[12,13]

Considerable effort has been expended in the development of mathematical models of microwave heating processes in 2-D[14] and 3-D[15–18] systems. These studies have shown that microwave absorption is not generally uniform throughout a system, but has a complex spatial distribution depending on the load and geometry, with the heating often concentrated in localized hot spots, or nodes, within the system. These hot spots can lead to buoyancy-driven free convection processes that tend to disperse the energy through the system, and simulations have shown that changes in the positions of the hot spots can lead to significant differences in the extent of the convective mixing.[19] Phase change behavior in microwave-heated systems has been studied by Basak et al.,[20–22] who noted that sample geometry can greatly affect thawing times owing to its effect on the temperature distributions within the system. Alpert et al.[23] showed that significant changes in the predicted evolution of heating profiles with time can occur when the effects of temperature-dependent dielectric properties are accounted for. Such effects can be very important in practical processing applications when the dielectric loss increases with temperature, as it does in aqueous salt solutions,[11] since, in principle, this situation can result in runaway heating, making the control of microwave processes difficult.[24,25] The majority of these models have employed finite element methods to simulate heating in the target systems, although with the availability of high-speed computers, molecular dynamics models can now be developed.[6] These model predictions, which indicate that microwave energy is not delivered to the target uniformly, and that hot spots develop within the heated material, have yet to be validated with experimental measurements of temperature distributions within microwave heated systems.

In contrast to the number of modeling efforts, there are comparatively few experimental temperature measurements in microwave cavities. One of the primary difficulties is that conventional methods for measuring temperature adversely affect the microwave distribution within the system, and are themselves affected by the presence of the microwaves. For this reason, Dibben et al.[26] were able to make 3-D temperature measurements within a sample using multiple metal thermocouples only after the cessation of the microwave irradiation. A common alternative to metal thermocouples is the fiberoptic thermometer, composed of an encased temperature-sensitive phosphor that is connected via fiber optics to the rest of the thermal monitoring system. Zhao et al.[27] and Wei et al.[4] used such fiber optic thermometers to make single-point measurements within their samples. Because microwave heating is volumetric in nature, however, point measurements do not adequately capture the temperature field. Experiments have also been conducted with infrared (IR) cameras to measure surface temperature distributions both after[28] and during[2,29] microwave heating. Because infrared radiation can be absorbed by the heated material, IR measurements are restricted to surfaces and cannot provide information on temperature variations within the sample volume. Recently, magnetic resonance imaging (MRI) techniques have been used to measure temperature distributions in microwave heating processes,[30–33] but these methods are slow and cannot be applied to standard microwave cavities, and are, therefore, limited in their utility for measuring temperature distributions in microwave heating applications.

The availability of techniques for measuring temperatures accurately in multiple dimensions in a sample under microwave irradiation is critical for validation of computer models of microwave heating processes. Such measurements should be made remotely, without disturbing the system, and, hence, should not entail the use of macroscopic physical probes. Molecular probes that exhibit temperature-sensitivity, and that can be dispersed dilutely throughout the irradiated sample satisfy these requirements, as the probes do not affect microwave absorption processes measurably, and, in principle, should not affect the transport processes within the sample being radiated. One approach is to use dilute solutions of a temperature-sensitive fluorescent dye for the remote optical measurement of temperature distributions, which can be monitored through changes in the spatial fluorescence intensities in a sample. The excitation energy for the fluorescence can be provided to a spatially isolated region, by using a laser beam that has been expanded along a single axis as a way to illuminate a specific plane within a 3-D region. This approach is the basis for planar-laser induced fluorescence (PLIF) methods. Using this strategy, the 2-D fluorescence patterns emitted normally to the illuminated plane are captured on an imaging camera, and, from the relative intensities of the fluorescence signals at different points in the system, spatial variations in temperature within this plane can be evaluated directly. This technique has been used successfully not only for 2-D temperature measurements,[34,35] but also for determinations of 2-D pH[36] and concentration profiles.[37] 3-D measurements of temperature[34] and concentration[38] profiles have also been demonstrated with PLIF, by moving the measurement plane in steps through the system.

In this work, we present the first demonstration of direct, *in situ* 2-D temperature measurements during microwave heating, and compare the initial heating patterns with those predicted by simulations of the irradiated sample within the microwave cavity. We summarize the development of our PLIF-based imaging thermometry instrument and present results on the evolution of temperature profiles in microwave heated water

and salt (NaCl) samples. We observed significant changes in the temperature profiles owing to the changes in dielectric properties at the different salt concentrations. A range of salt concentrations from 0 to 0.5 M was examined, and the initial heating profiles from these experiments compare favorably with simulation results obtained using a commercial finite element solver.

Materials and Methods

We designed a custom fluorimeter that could be integrated with a microwave cavity for the direct *in-situ* measurement of 2-D temperature profiles in a sample cell using molecularly-dispersed fluorescent temperature probes. A planar laser beam was used to isolate the measurement region by confining the excitation spatially to a 2-D plane within the sample. To minimize noise from temporal and spatial variations in the laser beam, two fluorescent dyes were used: one dye for temperature measurement, and the other, as a reference for the laser power intensity. The resulting 2-D fluorescence intensity patterns for the two dyes were resolved using suitable beam splitting and optical filtering, and captured by dual cameras. We provide a summary of the salient features of the experimental system below; more detailed descriptions are available elsewhere.[39]

Molecular probes

Rhodamine B (Laser Grade 98% purity from Fisher Chemical) is a fluorescent, temperature-sensitive, water-soluble xanthene compound, often used as a laser dye. The chemical properties of Rhodamine B have been studied extensively,[40–49] and its temperature-sensitivity (Figure 1a) has been utilized in a variety of applications.[34,50–52] It has an absorption peak at 554 nm with a fluorescence peak at 576 nm, and has a linear temperature response in emission intensity from 10–60°C.[34,52] Rhodamine B tends to adsorb onto glass and other surfaces,[34,48,49] and at low-concentrations (<1 μM), changes in probe concentration due to this adsorption can cause changes in fluorescence that are of the same order of magnitude as the fluorescence temperature response itself. This adsorption problem was overcome by using a dextran polymer labeled with Rhodamine B (10,000 MW anionic, 95% purity from Molecular Probes) instead of the pure dye. The attached dye has a red shifted spectrum, with an absorption peak at 571 nm, and a fluorescence peak at 590 nm, but shows no loss in its temperature sensitivity.

Rhodamine 110 (99% purity from Sigma-Aldrich), which has an absorption peak at 497 nm, a fluorescence emission peak at 519 nm, and a significantly lower temperature sensitivity than Rhodamine B (Figure 1a), was included as a reference to the Rhodamine B sample in order to account for intensity changes in the laser beam; since the emission intensities from the two dyes are each directly proportional to the excitation intensity, fluctuations in the beam intensity were cancelled out in the ratio of emission intensities from the two dyes at their respective absorption peaks. This ratio depends strongly on temperature, as shown in Figure 1b.

Microwave cavity

A commercially available microwave single mode cavity resonator plasma heater with orthogonal optical ports, shown in

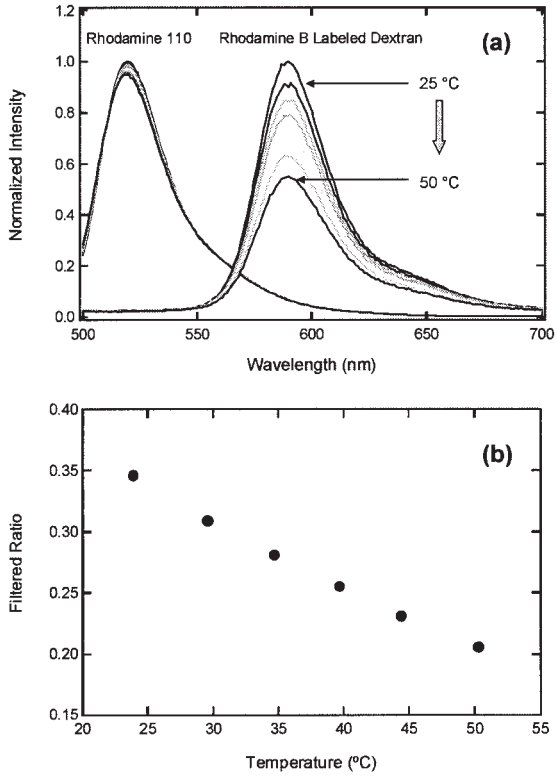

Figure 1. Temperature dependent fluorescence of Rhodamine B-labeled Dextran and Rhodamine 110.

(a) Fluorescence spectra; (b) temperature response of the ratio of Rhodamine B and Rhodamine 110 integrated fluorescent intensities.

Figure 2a, was purchased from Sairem and used as the microwave applicator. Microwave radiation at 2.45 GHz was generated using a Sairem GMP12K/SM 1.2 kW microwave generator, coupled with a CD1 isolator, MC1 3-stub tuner, SC3 single mode cavity and MC3 sliding short circuit. The cavity was a modified section of a rectangular (86.4 cm $\times$ 43.2 cm) microwave waveguide with a circular port on either side of the wide axis, and two smaller oval auxiliary ports located orthogonally to the circular ports, as shown in Figure 2. The 23.6 mm $\times$ 34 mm $\times$ 70 mm (HWD) silica glass sample cell (Figure 2b) was registered to the sample cell holder by a raised L-shaped guide (Figure 2c). The sample cell holder was moved manually and slid into the cavity until it hit a mechanical stop.

The laser illumination for the sample cell was provided by a Coherent Innova 90C argon-ion laser, and passed through a clear aperture in the bottom of the sample cell holder, shown in Figure 3. Due to the narrow aperture of the small optical ports used to introduce the excitation beam to the cavity, entire planar illumination of the sample cell cross section was not possible. A sequence of three plano convex cylindrical lenses—FL = 100 mm (Newport CKX100AR.14), FL = 200 mm (Newport CKX200AR.14), and FL = 25.4 mm (Newport CKX025AR.14)—shown in Figure 3, was used to shape the beam to illuminate as large a wedge-shaped segment within the sample cell as possible. These lenses produced a wedge with a maximum width of 25 mm and a depth of less than 3 mm. The photograph shows the illuminated plane, as seen through the

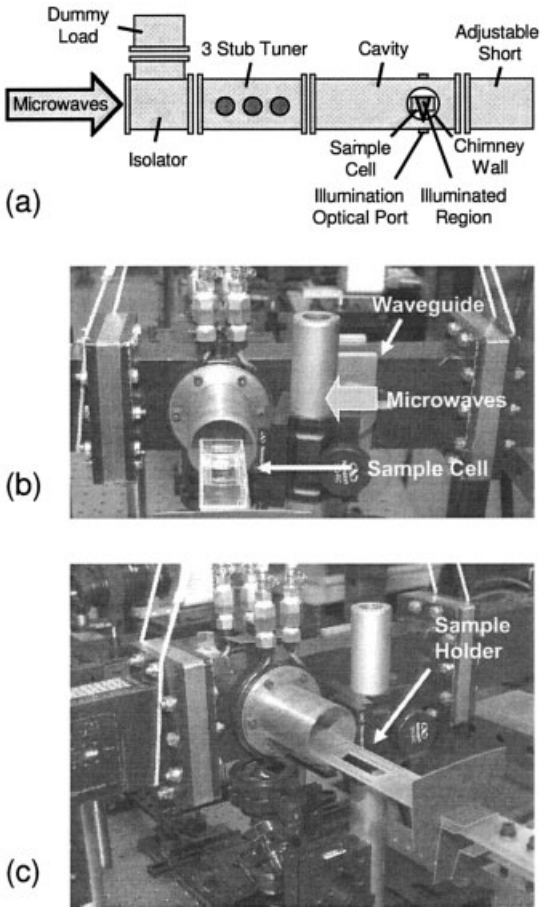

Figure 2. (a) Experimental microwave applicator showing location of the isolator, dummy load, tuner, cavity and short circuit. Optical ports for the introduction of the excitation beam and the observation of the emitted fluorescence signals are shown; (b) microwave cavity with sample cell prior to insertion; and (c) a view of the sample cell holder with opening for access by the laser.

larger optical ports used for imaging the fluorescence emission distributions.

Detection of the fluorescence signals was accomplished with a dual camera arrangement as shown in Figure 4. A dichroic mirror was used to split the fluorescence emission signal into two beams of differing wavelength ranges, each of which was then filtered to remove additional unwanted radiation. The two filtered images were captured on separate cameras, and provided independent maps of the Rhodamine 110 and Rhodamine B emission patterns. We employed Hamamatsu Orca ER CCD cameras with Nikon Micro Nikkor 105 mm AF lenses. The 550 nm dichroic mirror (Omega Optical XF2017) used in our system reflected wavelengths shorter than 550 nm into the Rhodamine 110 camera, and passed wavelengths longer than 550 nm into the Rhodamine B camera. Additional filters were attached to the cameras to suppress scattered light from the laser. A 560 nm long pass filter (CVI Laser Corp. CG-OG-570-2.00-3) was used to isolate the Rhodamine B fluorescence, while a 520 nm (10 nm FWHM, Oriel 54351) interference filter

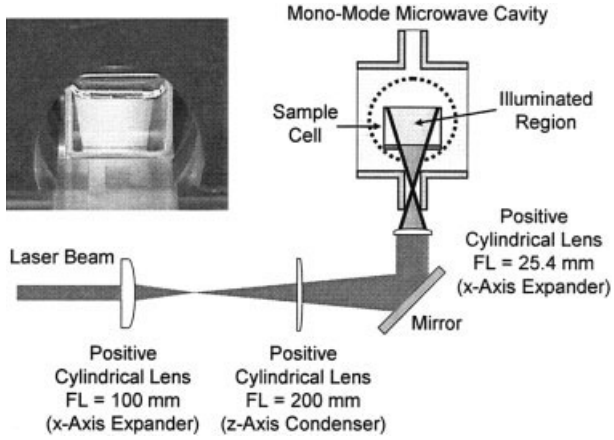

Figure 3. Laser optics design for PLIF illumination inside the microwave cavity.

Inset image shows actual illumination of a sample by the laser.

was used to isolate the Rhodamine 110 fluorescence. The image planes of the two cameras were matched by a combination of mechanical and electronic registration. A custom high-contrast image registration target composed of a pattern of dots was used to provide a reference point for the mathematical processing of the data using image registration tools in MATLAB.[39]

Complete optical separation of the fluorescence signals from the two dyes could not be achieved because of the overlap in their fluorescence spectra as seen in Figure 1a. We followed the mathematical treatment developed by Sakakibara et al.[34] to further resolve the fluorescence signals yielded by the two dyes. The fluorescence intensity I, can be expressed as

$$I = C\phi\varepsilon \tag{2}$$

where C is the concentration of the probe, ϕ is the temperature-dependent quantum yield, and ε is the extinction coefficient. Prior to any experiment, we conducted calibration runs with the two dyes individually to determine the response of each camera to the fluorescence of a specific dye. The ratio of the temperature-dependent quantum yields for a mixture of the two dyes can then be expressed as[34]

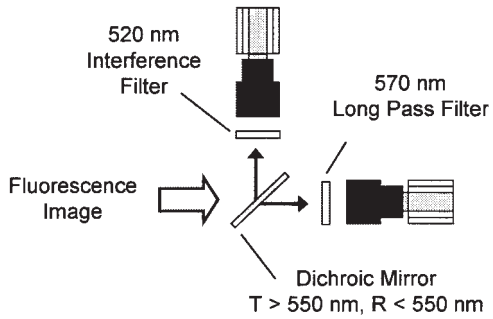

Figure 4. Optical filter and dichroic mirror arrangement for separation of Rhodamine B and Rhodamine 110 fluorescence signals and their recording by the two cameras.

$$\frac{\phi_B}{\phi_A} = \frac{A}{B}\left(\frac{V_A^\beta - RV_A^\alpha}{RV_B^\alpha - V_B^\beta}\right) \tag{3}$$

where V refers to the camera signal for the calibration experiments for any individual dye at a fixed temperature, and for a given position within the plane. The subscripts A and B refer to the specific dyes, and α and β superscripts designate the specific cameras. The variables A, B, and R are defined as

$$A = \frac{C_A}{C'_A\phi'_A},\ B = \frac{C_B}{C'_B\phi'_B},\ R = \frac{V^\beta}{V^\alpha} \tag{4}$$

The primes denote the conditions of the calibration experiment, and R is the ratio of the camera signals at a particular position within the plane for a mixture of the dyes during the experimental run. Equation 3 converts the ratio of the camera signals R, into a ratio of the quantum yields which, with a description of the temperature dependence of the quantum yield ratio for the probes, allowed the solution for temperature. With this approach, a temperature sensitivity of ± 1.6°C was achieved with an optical resolution of 123 μm. Greater temperature sensitivity is possible, and can be attained at the expense of optical resolution by binning or averaging measured intensities with a larger number of adjacent pixels.

Experimental procedure

Temperature distributions were measured as a function of time during the microwave heating of both pure water and salt solutions of varying concentrations (0.05–0.5 M). The microwave experiments were conducted at 2.45 GHz, the internationally recognized frequency for heating applications, with an input power of 400 W and a heating time of 25 s. The sample cell was filled with 30 mL of a solution with the fluorescent probes, Dextran-labeled Rhodamine B at 0.3 μM of the dye and Rhodamine 110 at 0.03 μM. The 488 nm laser line was used for excitation of the fluorescence at a power setting of 620 mW. The exposure time of the cameras was set to 100 ms, and the image capture rate was 2 Hz. Photobleaching of the dyes was minimized by employing a high-speed shutter to limit laser illumination of the sample to the camera exposure time. In any given experiment, the sample cell was loaded and allowed to equilibrate for 1.5 h. A sequence of 10 images was captured at room-temperature, and then the microwave was run for 25 s. The camera and laser shutter timing were controlled by a computer, and the microwave start and stop were triggered manually. Sixty images were captured in each experiment, and the room-temperature images were used as a reference point for temperature calibration.

Results and Discussion

Interpretation of the experimental images

Figure 5 shows a typical image obtained during the microwave heating of a water sample placed in the rectangular cell located centrally within the waveguide. The laser light entered from the bottom of the sample cell (see Figure 3), and illuminated a wedge shaped subsection of the central plane within the cell, resulting in fluorescence images that were obtained perpendicularly to the axes of both the illumination and the microwave irradiation. The upper portion of each collected image (Figure 5) was bounded by a meniscus that acted as a lens and disrupted measurements in that region. The dark-side regions were not directly illuminated, but were subject to a diffuse illumination from scattered light within the cavity that provided some excitation of the dyes in that region. The sample was irradiated with microwaves from the left of the cell, but reflections within the cavity created an electric field distribution that was not limited to the leading edge of the sample. Nonhomogeneous heating occurred throughout the sample, with the local energy input rates determined by the dielectric properties of the sample, the cavity geometry, and the field distribution within the cell. The blue regions indicate temperatures close to ambient, and yellow and red denote elevated temperatures. Clearly, the microwave heating was not uniform, and was concentrated in isolated hot spots, or nodes. In this example, two dominant nodes were observed to be almost symmetrical about the vertical centerline, while smaller nodes were observed near the center at the top and bottom of the cell. We can also discern large qualitative changes in temperature in the dark zones, although we were unable to make accurate temperature measurements in these regions because of the signal to noise levels. In particular, we noted a heated node at the corner of the leading edge of the cell, and the clear outline of the trailing dominant node in the right hand dark zone; in these cases, the diffuse scattered light stimulated the observed weak fluorescence.

Experimental results

The experimental results for the time evolution of microwave heating patterns in the sample cell placed at the center of the waveguide are shown in Figure 6 for a range of salt concentrations. The early temperature distributions, at $t = 2.5$ s, show a consistent trend of concentrated heating in nodes for all solutions. With increasing salt concentrations, however, the nodes shifted towards the incident face of the microwave radiation. The increased asymmetry in the distribution of the hot spots at the higher salt concentrations was a direct result of the increased solution conductivity, and, hence, effective dielectric loss, leading to increased microwave absorption near the leading wall, and, hence, limited microwave penetration into the sample. By the same token, the resonance in the microwave cavity was reduced, and less microwave power was reflected back into the sample from the far wall of the cell. By an exposure time of $t = 3.5$ s, salt concentration dependent flow patterns had developed within the cell owing to buoyancy-driven free convection. The heated nodes were less dense than the surrounding, cooler fluid, and rose to the upper surface of the cell (the meniscus), where they were deflected sideways. When the plumes from the two heated nodes collided, they were deflected downwards to give the characteristic mushroom-like structure observed at 3.5 s. In pure water, the mushroom formation arose from the major heating nodes, with the leading node dominating, as is evident from the relative magnitudes of the two mushroom patterns. With increases in salt concentration, the decrease in the intensity of the trailing node presaged the disappearance of the trailing mushroom, until, at the higher salt concentrations, only one heated zone was observed and, on deflection at the meniscus surface, it traversed the entire width of the cell before hitting the far wall and

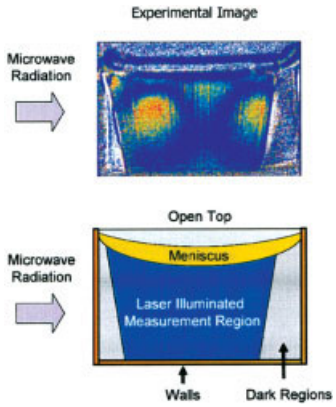

Figure 5. Illuminated sample cell (lower) with representative experimental image obtained using PLIF (upper).

sinking. By $t = 7.5$ s the convective processes had slowed considerably, and a more uniform, vertically-stratified temperature distribution had been established. The final recorded images at $t = 25$ s shown in Figure 7 (note the different temperature scale from that used in Figure 6) continued to show this fairly uniformly stratified temperature distribution, albeit with some residual embedded structure of the heating nodes. The higher-temperatures reported in Figure 7 are consistent with the absorption of more microwave energy over a longer period of time. It is interesting to note that in both Figures 6 and 7 the uniformity of heating in the 0.5 M NaCl solution was less than in solutions of lower-salt concentration, despite the fact that the dielectric loss is higher for higher-salt concentrations. This effect occurred because only a narrow region of the solution near the incident face of the cell was heated, and the resulting plume was sufficiently hot relative to

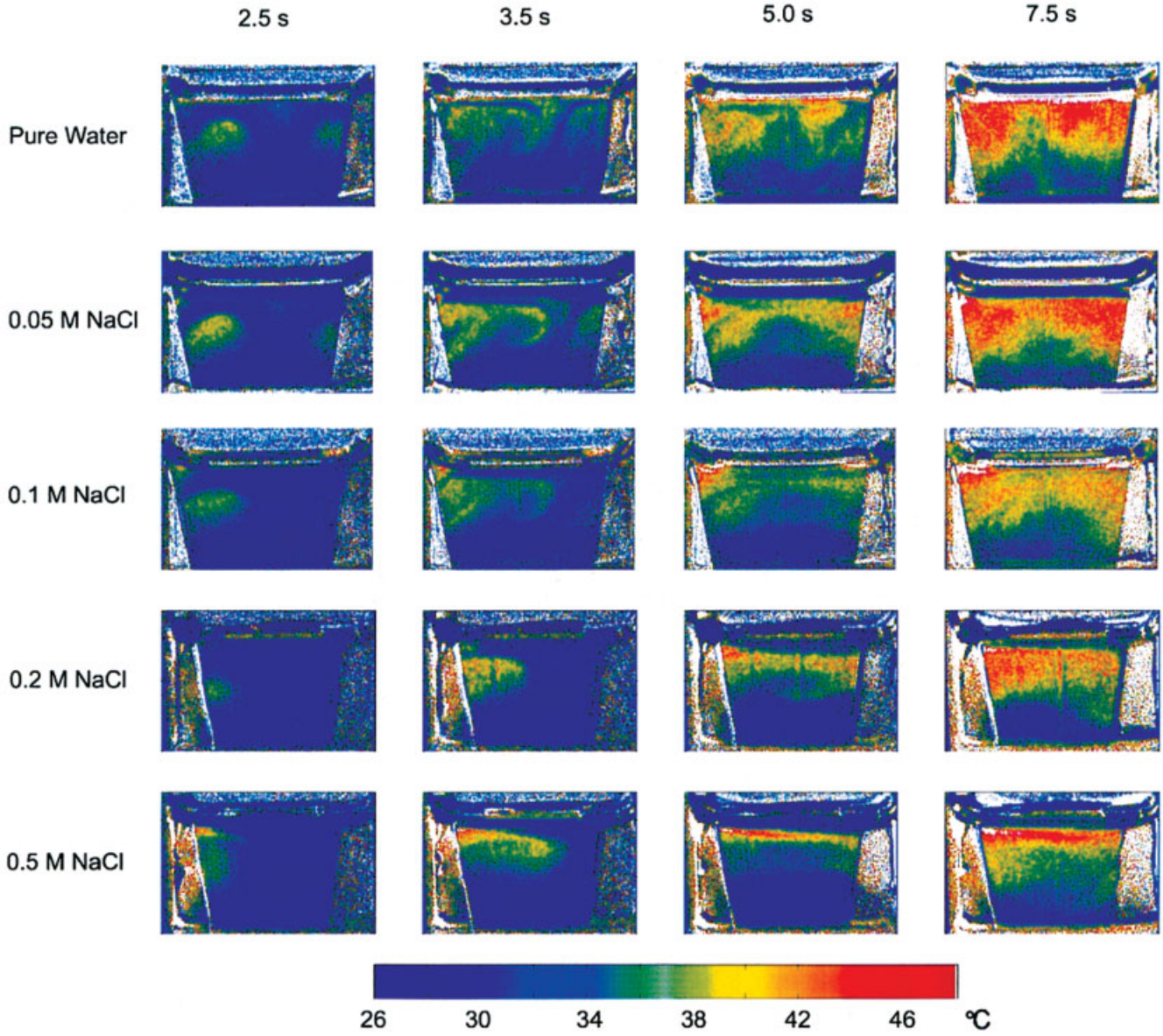

Figure 6. Experimental results showing measured temperature profiles produced by microwave heating of different concentrations of NaCl in water during the first 7.5 s of heating.

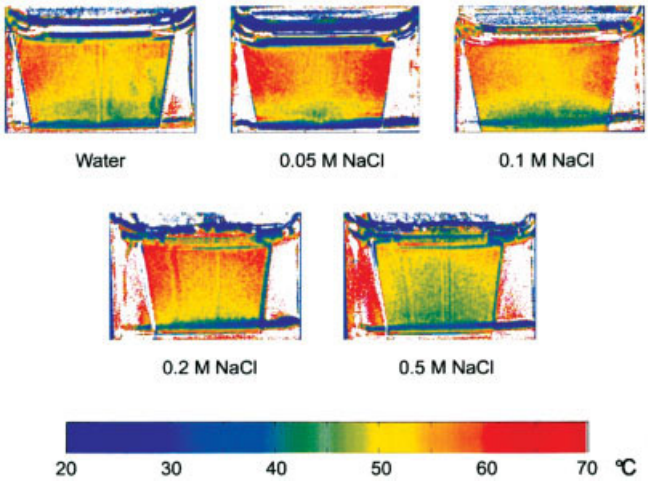

Figure 7. Final temperature distributions in the sample cell for different concentrations of NaCl in water after 30 s of microwave heating.

(Note: The temperature color scale is different from Figure 6.)

the surrounding fluid that it did not sink again when it hit the far wall, but remained near the meniscus surface.

The images shown in Figures 6 and 7 are characterized by an increasing distortion in the temperature patterns with time in the form of vertical lines. Scattered light was reflected, albeit rather weakly, from the two vertical walls, which formed a resonant cavity or etalon, and established an interference pattern in the laser light as it illuminated the sample. Slight mechanical errors in positioning of the sample cell, and the thermal expansion of the glass cell walls during the microwave heating changed the interference pattern formed by the etalon and resulted in an optical anomaly in the form of lines running parallel to the laser beam path caused by dividing two images with slightly mismatched interference pattern positions. The thermal expansion of the cell wall altered the interference pattern over time and, as seen in Figure 6, the strength of the lines increased as the cell temperature changed. The line structure is strongest at the centerline, because the effects are most prominent where the laser beam is perpendicular to the sample cell floor.

These experimental observations show strong nonuniform heating effects, and demonstrate the utility of PLIF for the dynamic, remote monitoring of full 2-D temperature profiles in microwave heated samples. We demonstrate below that the observed initial temperature distributions, and their variation with salt concentration are consistent with models of microwave power distributions in cavities of the geometry considered here.

Table 1. Material Properties Used in the 2-D Model of the Microwave Cavity

	Real Relative Dielectric Constant (ε')	Conductivity (σ) (S/m)
Water	78.34	0.002
0.05 M Salt	77.36	0.514
0.1 M Salt	76.39	1.016
0.2 M Salt	74.51	1.989
0.5 M Salt	69.3	4.68

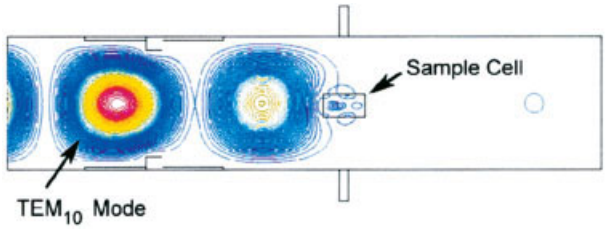

Figure 8. Calculated electric field distribution in the microwave waveguide, in which the incident microwave radiation is applied from the left.

Model prediction of temperature distributions in microwave heated solutions

We estimate the temperature distributions within the sample volume by noting that the local power intensity is a good indicator of the relative heating rates at any point within a microwave heated sample.[15] The rate at which heat is delivered to the sample due to microwave absorption is given by

$$Q = \frac{1}{2}\,\omega\varepsilon'' E \cdot E^* \tag{5}$$

where ω is the angular frequency of the microwaves, E is the electric field strength, and E^* its complex conjugate. This equation, derived from the Poynting theorem,[5] shows that microwave heating depends only on the electric field compo-

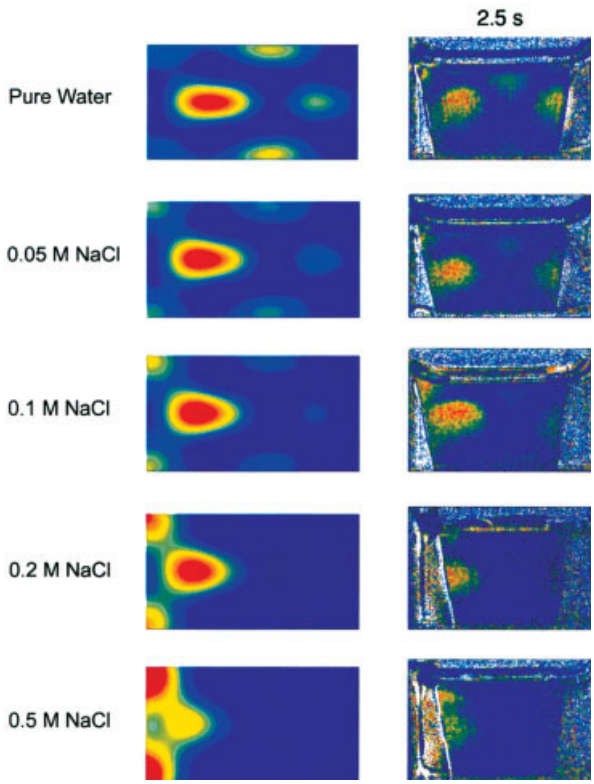

Figure 9. Simulation (left column) and experimental results (right column) for early time temperature profiles within microwave-heated aqueous solutions of different concentrations of NaCl.

nent of the electromagnetic wave. We used a commercial CFD package, FEMLAB, to solve the set of Maxwell equations for the electric-field strength distribution in the microwave guide, and the sample subject to appropriate boundary conditions. Specifically, the microwaves were modeled in 2-D with the magnetic field component in the plane of the simulation, and the electric field component normal to this plane. The walls were modeled as perfect conductors, and continuity was observed at the dielectric interface. A temperature-independent, homogeneous dielectric constant was assumed.

A full description of microwave heating would require a coupling, through Eq. 5, of the solution to the Maxwell equations with the equations of continuity for heat, mass, and momentum to allow for conductive and convective heat transfer in the system.[2] In this work, however, we investigated only the initial heating patterns before thermal conduction and buoyancy driven flows affected the overall temperature distributions, that is, we ignored thermal conduction and fluid-flow effects. Simulations were performed for water, and the four-salt solutions (0.05 M, 0.1 M, 0.2 M, 0.5 M) used in the experimental program. The dielectric properties of salt water solutions were computed using the relations developed by Stogryn[11] (Table 1), with the effective dielectric loss ε'', estimated by

$$\varepsilon''_{effective} = \frac{(\varepsilon'_L - \varepsilon'_H)\omega\tau}{1 + \omega^2\tau^2} + \frac{\sigma}{\varepsilon_0\omega} \tag{6}$$

Here, ε'_L is the low-frequency real relative dielectric constant tabulated in Table 1, ε'_H is the high-frequency limit real relative dielectric constant, taken to be 4.9,[11] σ is the solution conductivity, and ε_0 is the permittivity of free space. The relaxation time of water τ, has been given as 8.1 ps.[11]

The electric field for the TEM_{10} mode in the waveguide in the simulation geometry of the microwave applicator is shown in Figure 8. The higher permittivity of the sample cell deformed the electric field pattern to allow for regions of higher electric field strength within the sample, which corresponded to the heated, elevated temperature nodes. The decreased field intensity of the electric field upstream (that is, to the left) of the sample cell indicated that the microwave input power was absorbed by the sample, while the lack of significant field contours downstream of the cell showed reflection of power away from the sample.

The calculated relative power intensities within the sample cell are compared with the corresponding experimental temperature distributions after 2.5 s of exposure to the microwave radiation in Figure 9. There was no significant motion of the heated nodes at this point, and sufficient time had elapsed to ensure the establishment of significant temperature differences between the heated and unheated regions. The simulation for pure water shows six heating nodes, four of which are prominent, with the leading edge node clearly being the strongest. The five nodes within the field of view in the experiment all appear in the locations predicted by the simulations. The mismatch between the predicted intensities of the nodes at the top and bottom of the sample cell, and the experimental observations may be due to approximations inherent in the model used, as the electric field is very sensitive to system geometry and the boundary conditions used in the simulation. The intensities of the simulated heating nodes shifted to favor those closer to the incident face for microwave radiation with increases in the salt concentration. By 0.2 M salt concentration, there was no significant heating in the top, bottom, and trailing nodes. The corner nodes at the left edge continued to rise in intensity until they dominated at 0.5 M salt concentration. Note that these heating patterns were evident even in the regions on either side of the wedge that were not directly illuminated. The shift in prominence of heating nodes, as seen in the simulation, was matched closely by the changes observed in the experiments, giving confidence in the reliability of our experimental approach for the dynamic monitoring of temperature distributions in microwave heated systems.

Conclusions

Research and development on industrial applications of microwave heating have been hampered by the lack of experimental methods to verify increasingly sophisticated models of microwave absorption and dissipation processes. In this work, we have demonstrated the first application of fluorescent temperature probes to the direct *in situ,* and real-time measurement of heating patterns in a microwave cavity. These results are in contrast to previous studies, where bulk measurements were made after microwave heating. We integrated the optical technique of planar laser-induced fluorescence (PLIF), with a microwave cavity containing a rectangular sample cell filled with pure water or a salt solution. Two fluorescent dyes, Rhodamine B and Rhodamine 110, were used with a dual camera imaging system to resolve 2-D temperature patterns to within ± 1.6°C at a spatial resolution of 123 μm. The time-dependent microwave heating patterns observed experimentally for water solutions of varying salt concentration showed characteristic, intensely-heated, spatially distributed nodes surrounded by regions in which little or no microwave absorption occurred. These nodes were increasingly displaced asymmetrically towards the incident face of the cell with increasing salt concentration, owing to the increased conductivity of these solutions. The initial heating profiles in these experiments prior to the onset of buoyancy-driven convection and heat transfer were in good agreement with a simplified model of the electric field power-intensity distribution in the waveguide. With time, buoyancy-driven convective flow patterns were established that lead to vertically-stratified, almost horizontally uniform, temperature distributions within the samples. An important consequence of this observation is that microwave heating can lead to significant long-range temperature nonuniformities that can have a profound impact on, for instance, selectivities and yields of microwave-heated reaction systems.

Acknowledgements

This work was supported by grants from NSF and EPRI. The authors thank Peter So for a number of insightful discussions and Dan Ehrlich for the loan of some optical equipment.

Literature Cited

1. Roy R, Agrawal D, Cheng JP, Mathis M. Microwave Processing: Triumph of Applications Driven Science in WC-Composites and Ferroic Titanates. In: Clark DE, Sutton WH, Lewis DA, eds. *Microwaves: Theory and Application in Materials Processing IV.* Vol 80: Ceramics Trans.; 1997:3–26.
2. Ratanadecho P, Aoki K, Akahori M. A numerical and experimental investigation of the modeling of microwave heating for liquid layers using a rectangular wave guide (effects of natural convection and dielectric properties). *Appl Math Modelling.* 2002;26(3):449–472.
3. Stuerga DAC, Gaillard P. Microwave athermal effects in chemistry: A myth's autopsy. 1. Historical background and fundamentals of wave-

matter interaction. *J of Microwave Power and Electromagnetic Energy.* 1996;31(2):87–100.
4. Wei CK, Davis HT, Davis EA, Gordon J. Heat and mass transfer in water-laden sandstone: Microwave heating. *AIChE J.* 1985;31(5):842–848.
5. Ayappa KG. Modelling transport processes during microwave heating: A review. *Reviews in Chem Eng.* 1997;13(2):1–69.
6. English NJ, MacElroy JMD. Molecular dynamics simulations of microwave heating of water. *J of Chem Phys.* 2003;118(4):1589–1592.
7. Zasetsky AY, Svishchev IM. Dielectric response of concentrated NaCl aqueous solutions: Molecular dynamics simulations. *J of Chem Phys.* 2001;115(3):1448–1454.
8. Buchner R, Hefter GT, May PM. Dielectric relaxation of aqueous NaCl solutions. *J of Phys Chem A.* 1999;103(1):1–9.
9. Nortemann K, Hilland J, Kaatze U. Dielectric properties of aqueous NaCl solutions at microwave frequencies. *J of Phys Chem A.* Sept 11. 1997;101(37):6864–6869.
10. Stogryn A, Desargant GJ. The dielectric-properties of brine in sea ice at microwave-frequencies. *IEEE Transactions on Antennas and Propagation.* 1985;33(5):523–532.
11. Stogryn A. Equations for calculating the dielectric constant of saline water. *IEEE Transactions on Microwave Theory and Techniques.* 1971;MTT-19:733–736.
12. Lou JF, Paravastu AK, Laibinis PE, Hatton TA. Effect of temperature on the dielectric relaxation in solvent mixtures at microwave frequencies. *J of Phys Chem A.* Dec 18. 1997;101(51):9892–9899.
13. Lou JF, Hatton TA, Laibinis PE. Effective dielectric properties of solvent mixtures at microwave frequencies. *J of Phys Chem A.* 1997; 101(29):5262–5268.
14. Ayappa KG, Davis HT, Davis EA, Gordon J. Two-dimensional finite element analysis of microwave heating. *AIChE J.* 1992;38(10):1577–1592.
15. Zhao H, Turner IW. An analysis of the finite-difference time-domain method for modeling the microwave heating of dielectric materials within a three-dimensional cavity system. *J of Microwave Power and Electromag Energy.* 1996;31(4):199–214.
16. Harms PH, Chen Y, Mittra R, Shimony Y. Numerical modeling of microwave heating systems. *J of Microwave Power and Electromag Energy.* 1996;31(2):114–121.
17. Liu F, Turner I, Bialkowski M. A finite-difference time-domain simulation of power-density distribution in a dielectric-loaded microwave cavity. *J of Microwave Power and Electromag Energy.* 1994;29(3):138–148.
18. Jia X, Jolly P. Simulation of microwave field and power distribution in a cavity by a 3-dimensional finite-element method. *J of Microwave Power and Electromag Energy.* 1992;27(1):11–22.
19. Ayappa KG, Brandon S, Derby JJ, Davis HT, Davis EA. Microwave driven convection in a square cavity. *AIChE J.* 1994;40(7):1268–1272.
20. Basak T, Ayappa AG. Analysis of microwave thawing of slabs with effective heat capacity method. *AIChE J.* 1997;43(7):1662–1674.
21. Basak T, Ayappa KG. Influence of internal convection during microwave thawing of cylinders. *AIChE J.* 2001;47(4):835–850.
22. Basak T, Ayappa KG. Role of length scales on microwave thawing dynamics in 2D cylinders. *Intl J of Heat and Mass Transfer.* 2002; 45(23):4543–4559.
23. Alpert Y, Jerby E. Coupled thermal-electromagnetic model for microwave heating of temperature-dependent dielectric media. *IEEE Transactions on Plasma Sci.* 1999;27(2):555–562.
24. Wu X, Thomas JR, Davis WA. Control of thermal runaway in microwave resonant cavities. *J of Appl Phys.* 2002;92(6):3374–3380.
25. Hill JM, Marchant TR. Modelling microwave heating. *Appl Math Modelling.* 1996;20(1):3–15.
26. Dibben DC, Metaxas AC. Finite element time domain analysis of multimode applicators using edge elements. *J of Microwave Power and Electromag Energy.* 1994;29(4):242–251.
27. Zhao H, Turner IW. The use of a coupled computational model for studying the microwave heating of wood. *Appl Math Modelling.* 2000; 24(3):183–197.
28. Jia X. Experimental and numerical study of microwave-power distributions in a microwave-heating applicator. *J of Microwave Power and Electromag Energy.* 1993;28(1):25–31.
29. Rattanadecho P, Aoki K, Akahori M. Experimental validation of a combined electromagnetic and thermal model for a microwave heating of multi-layered materials using a rectangular wave guide. *J of Heat Transfer-Transactions of the ASME.* 2002;124(5):992–996.
30. Bows JR, Patrick ML, Nott KP, Hall LD. Three-dimensional MRI mapping of minimum temperatures achieved in microwave and conventional food processing. *Intl J of Food Sci and Technol.* 2001;36(3):243–252.
31. Nott KP, Hall LD, Bows JR, Hale M, Patrick ML. MRI phase mapping of temperature distributions induced in food by microwave heating. *Magnetic Resonance Imaging.* 2000;18(1):69–79.
32. Nott KP, Hall LD, Bows JR, Hale M, Patrick ML. Three-dimensional MRI mapping of microwave induced heating patterns. *Intl J of Food Sci and Technol.* 1999;34(4):305–315.
33. Behnia B, Suthar M, Webb AG. Closed-loop feedback control of phased-array microwave heating using thermal measurements from magnetic resonance imaging. *Concepts in Magnetic Resonance.* 2002; 15(1):101–110.
34. Sakakibara J, Adrian RJ. Whole field measurement of temperature in water using two-color laser induced fluorescence. *Experiments in Fluids.* 1999;26(1–2):7–15.
35. Lee MP, McMillin BK, Hanson RK. Temperature measurements in gases by use of planar laser-induced fluorescence imaging of NO. *Applied Optics.* 1993;32(27):5379–5396.
36. Coppeta J, Rogers C. Dual emission laser induced fluorescence for direct planar scalar behavior measurements. *Experiments in Fluids.* 1998;25(1):1–15.
37. Hanson RK. Planar laser-induced fluorescence. *J of Quantum Spectroscopic Radiation Transfer.* 1988;40(3):343–362.
38. Island TC, Patrie BJ, Mungal MG, Hanson RK. Instantaneous three-dimensional flow visualization of a supersonic mixing layer. *Experiments in Fluids.* 1996;20(4):249–256.
39. Finegan TM. *Remote Three-Dimensional Temperature Sensing Using Planar Laser Induced Fluorescence: Development and Applications to Microwave Heated Liquids.* Cambridge: Chemical Engineering, Massachusetts Institute of Technology; 2004. PhD. Thesis.
40. Arbeloa TL, Estevez MJT, Arbeloa FL, Aguirresacona IU, Arbeloa IL. Luminescence properties of rhodamines in water-ethanol mixtures. *J of Luminescence.* 1991;48–9:400–404.
41. Arbeloa FL, Arbeloa TL, Estevez MJT, Arbeloa IL. Photophysics of rhodamines-molecular-structure and solvent effects. *J of Phys Chem.* 1991;95(6):2203–2208.
42. Arbeloa FL, Ojeda PR, Arbeloa IL. Fluorescence self-quenching of the molecular-forms of rhodamine-B in aqueous and ethanolic solutions. *J of Luminescence.* 1989;44(1–2):105–112.
43. Arbeloa IL, Rohatgimukherjee KK. Solvent effects on the photophysics of the molecular-forms of rhodamine-B internal-conversion mechanism. *Chem Phys Letts.* 1986;129(6):607–614.
44. Arbeloa IL, Ruizojeda P. Molecular-forms of rhodamine-B. *Chem Phys Letts.* 1981;79(2):347–350.
45. Casey KG, Quitevis EL. Effect of solvent polarity on nonradiative processes in xanthene dyes—Rhodamine-B in normal alcohols. *J of Phys Chemistry.* 1988;92(23):6590–6594.
46. Deshpande AV, Namdas EB. Lasing action of rhodamine B in polyacrylic acid films. *Appl Phys B-Lasers and Optics.* 1997;64(4):419–422.
47. Kubin RF, Fletcher AN. Fluorescence quantum yields of some rhodamine dyes. *J of Luminescence.* 1982;27(4):455–462.
48. Snare MJ, Treloar FE, Ghiggino KP, Thistlethwaite PJ. The photophysics of rhodamine-B. *J of Photochem.* 1982;18(4):335–346.
49. Ross D, Gaitan M, Locascio LE. Temperature measurement in microfluidic systems using a temperature-dependent fluorescent dye. *Analytical Chemistry.* 2001;73(17):4117–4123.
50. Lemoine F, Wolff M, Lebouche M. Simultaneous concentration and velocity measurements using combined laser-induced fluorescence and laser Doppler velocimetry: Application to turbulent transport. *Experiments in Fluids.* 1996;20(5):319–327.
51. Lemoine F, Antoine Y, Wolff M, Lebouche M. Simultaneous temperature and 2D velocity measurements in a turbulent heated jet using combined laser-induced fluorescence and LDA. *Experiments in Fluids.* 1999;26(4):315–323.
52. Gallery J, Gouterman M, Callis J, Khalil G, McLachlan B, Bell J. Luminescent thermometry for aerodynamic measurements. *Reviews of Scientific Instruments.* 1994;65(3):712–720.

Manuscript received Oct. 16, 2005, and revision received Apr. 15, 2006.